PCCP

ROYAL SOCIETY OF CHEMISTRY

PAPER

View Article Online
View Journal

Cite this: DOI: 10.1039/d6cp00964f

Formation and photolysis of multifunctional organic nitrates from the reaction of limonene and NO_3 radicals

Laura Wüst,[a] Lasse Moormann,[ab] Patrick Dewald,[a] Eunyeong Jin,[a] Jan Schuladen,[a] Jonathan Williams,[a] Frank Drewnick,[b] Ulrich Pöschl,[b] Jos Lelieveld[a] and John N. Crowley*[a]

Received 16th March 2026,
Accepted 26th April 2026

DOI: 10.1039/d6cp00964f

rsc.li/pccp

Multifunctional organic nitrates (LIM-ONO_2) were formed from the NO_3-initiated oxidation of limonene in the Simulation Chamber for Atmospheric Reactions and Kinetics (SCHARK), detected quantitatively by thermal dissociation cavity ring-down spectroscopy (TD-CRDS) and identified by high-resolution time-of-flight chemical-ionization (iodide) mass spectrometry (HR-ToF-ICIMS). Based on HR-ToF-ICIMS signal intensities, the most abundant LIM-ONO_2 were $C_{10}H_{17}NO_4$ and $C_{10}H_{17}NO_5$, together representing >60% of the total LIM-ONO_2 signal. We developed a method for cold-trapping LIM-ONO_2 from the chamber, enabling us to examine their photolysis in the absence of precursor chemicals after re-injection into the SCHARK. The photolytic loss frequency of $C_{10}H_{17}NO_4$ in the chamber when irradiated with LEDs emitting at 370 ± 13 nm was (1.69 ± 0.06) × 10^{-4} s^{-1}. By comparison to the photolysis frequency of a chemical actinometer (Cl_2), we were able to gain insight into the quantum yield (0.3–0.8) and absorption cross section of $C_{10}H_{17}NO_4$ at these wavelengths and make an estimate of its atmospheric lifetime with respect to photolysis.

1. Introduction

The oxidation of volatile organic compounds (VOCs) influences both air quality and climate through processes such as tropospheric ozone (O_3) formation and secondary organic aerosol (SOA) production.[1] Around 90% of all VOC emitted are biogenic, and the total global emissions of these biogenic volatile organic compounds (BVOCs) is estimated at ~1000 Tg per year, with monoterpenes accounting for ~5% of the total.[2] Although the contribution of monoterpenes to total BVOC emissions is small, they are highly reactive towards key atmospheric oxidants (*e.g.* O_3, OH and NO_3) and potent producers of new particles. While OH-initiated oxidation dominates during the daytime, NO_3 radicals (formed by the reaction of O_3 with NO_2, R1) play a central role in BVOC removal at night. These reactions lead to the formation of organic nitrates ($RONO_2$, R2), which act as a temporary reservoir for reactive nitrogen.[3–8] or can represent a permanent sink for NO_x when organic nitrates partition into the particle phase and are removed *via* deposition[9] or hydrolysis.[10–12] During the day, NO_3 undergoes rapid photolysis or reacts with NO to form NO_2[6] which drastically reduces its lifetime. In environments (*e.g.* forested regions) with high levels of BVOCs, NO_3 may contribute to their oxidation during the daytime.[13–15]

$$NO_2 + O_3 \rightarrow NO_3 + O_2 \quad (R1)$$

$$NO_3 + VOC + (O_2) \rightarrow RONO_2 + products \quad (R2)$$

There are several reaction steps between the initial formation of the nitrated organic radical (the product of electrophilic addition of NO_3 to a double bond in the BVOC) and the formation of stable, multifunctional organic nitrates. The identity of the stable end-products depends on the fate of the nitrated peroxy radicals (RO_2) formed when the nitrated organic radical reacts with O_2. RO_2 can react with NO, NO_3, other peroxy radicals or undergo auto-oxidation. In our experiments, even though NO_3 radicals initiate the oxidation of limonene, their mixing ratios are strongly suppressed by the high limonene mixing ratio and RO_2 + NO_3 reactions are not expected to play an important role. As there is no NO source in our chamber (under the dark conditions in which LIM-ONO_2 are formed) and the reaction with NO_2 forms thermally unstable peroxy nitrates that readily dissociate back to reactants, most products are expected to form in RO_2 + RO_2 type

[a] Atmospheric Chemistry Department, Max Planck Institute for Chemistry, Mainz, 55128, Germany. E-mail: john.crowley@mpic.de
[b] Multiphase Chemistry Department, Max Planck Institute for Chemistry, Mainz, 55128, Germany

reactions. RO_2 + HO_2 reactions are expected to be of minor importance for our system.

The chemical mechanisms involved in monoterpene degradation have not yet been fully characterized for most commonly emitted monoterpenes and the available literature does not provide a comprehensive understanding of organic nitrate formation pathways or their contribution to SOA composition and NO_x removal.[3] This is particularly pronounced for limonene, a monoterpene prevalent in urban, forested and indoor environments.[16,17] Limonene is highly reactive towards NO_3 radicals, with a rate coefficient of 1.2×10^{-11} cm^3 molecule^{-1} s^{-1} at 298 K.[18] By comparison, the rate coefficients for NO_3 + α-pinene (6.2×10^{-12} cm^3 molecule^{-1} s^{-1} at 298 K) and NO_3 + isoprene (6.5×10^{-13} cm^3 molecule^{-1} s^{-1} at 298 K) are much lower.[18] The reaction of NO_3 with limonene leads to the formation of long-chain multifunctional organic nitrates, many of which can partition into the particle phase or contribute to SOA formation.[19–22] Experimental studies have identified a variety of oxidation products from the limonene + NO_3 reaction, including hydroxy nitrates, carbonyl nitrates and hydroperoxy nitrates, which have been detected in both the gas and particle phases.[23–25]

The photolysis of organic nitrates derived from biogenic trace gases such as isoprene and α-pinene has been identified as a potential loss process that directly affects the abundance of reactive nitrogen in the atmosphere. If photolysis occurs after the organic nitrates have undergone long distance transport, reactive nitrogen can be released in remote areas where ozone production efficiency is high. Many $RONO_2$ species absorb dissociatively in the actinic region, releasing *e.g.* NO_2 and multifunctional alkoxy radicals (R3) that lead to further, organic oxidation products.[10,26–28] Experimental and theoretical studies have shown that the photochemical behaviour of organic nitrates strongly depends on their molecular structure. Measurements of Roberts and Fajer[29] and Barnes *et al.*[30] provided UV absorption cross sections for simple alkyl nitrates and a series of difunctional organic nitrates, including C3–C4 carbonyl nitrates and dinitrates. Barnes *et al.*[30] demonstrated that the UV-absorption spectra of carbonyl-substituted (keto) nitrates are red-shifted relative to non-substituted alkyl nitrates and have a factor five higher absorption cross sections at wavelengths above 290 nm. Subsequent work by Muller *et al.*[27] and Xiong *et al.*[26] demonstrated that conjugated nitrooxy carbonyl compounds formed from isoprene oxidation exhibit strong absorption in the near-UV region and undergo rapid photolysis under atmospherically relevant conditions.

Muller *et al.*[27] further showed that α- or β-nitrooxy carbonyl groups in isoprene derived nitrates enhance UV absorption and result in photolysis rates 3–20 times higher than those for OH loss. Xiong *et al.*[26] studied the photolysis of the isoprene-derived 4,1-nitrooxy-enal, a conjugated carbonyl-nitrate, and showed that conjugation between the carbonyl and nitrate functional groups enhances absorption in the actinic region, resulting in efficient photolysis with daytime atmospheric lifetimes of less than one hour. These findings highlight that certain conjugated carbonyl nitrates originating from BVOCs are highly photolabile and that photolysis can represent a major daytime sink for this class of compounds. Recent work by Wang *et al.*[31] has demonstrated that multifunctional organic nitrates (from α-pinene, β-pinene and limonene) can photolyse efficiently under actinic radiation, thereby reforming NO_x.

$$RONO_2 + h\nu \rightarrow NO_2 + RO \quad (R3)$$

Despite the potential importance of photolysis as a loss mechanism for atmospheric organic nitrates of biogenic origin, information regarding the photolytic lifetimes of such nitrates and their relative importance compared to *e.g.* deposition[9,14] or hydrolysis[32] remains sparse.

One factor that has hindered research into the photochemical degradation of atmospherically relevant organic nitrates is the difficulty of synthesizing the multifunctional nitrates involved. As a result, mainly surrogate species with similar structures have been examined so far.[26,27,31,33,34] In this study, we generate atmospheric organic nitrates (LIM-ONO_2) in the gas-phase *via* NO_3 induced oxidation of limonene in a simulation chamber, isolate them from precursor molecules by sampling into a cold-trap and then re-inject them into a precursor-free chamber to examine their behaviour during photolysis. Our goal is to produce the first dataset on the photolysis of selected LIM-ONO_2 species and to estimate their photodissociation quantum yields and atmospheric lifetimes.

2. Experimental

2.1. SCHARK chamber

The Simulation Chamber for Atmospheric Reactions and Kinetics (SCHARK) was used for the measurements described here. This cubic chamber (side length 1 m) is made of PFA film (0.13 mm thick) and has a volume of 1 m^3. The volume surrounding the PFA film is permanently flushed with dry-zero air to minimize contamination from laboratory air and the permeation of water vapour. Gases entering the chamber pass through a circular loop of perforated PFA tubing (10 holes of 1 mm diameter) located at the bottom of the chamber. Together with a magnetically coupled Teflon-coated fan, the gas-jets thus created, result in complete mixing in 40 s.[35] The chamber was operated at ambient pressure and temperature (298 ± 5 K) in dynamic-flow mode. The exchange constant (k_{exch}) of the chamber was determined by following the exponential decrease in the concentration of O_3 that had been injected into the chamber and is given by k_{exch} (s^{-1}) = 1.82×10^{-5} F, where F is the mass flow rate into the chamber in standard litres per minute (SLM).[36] The uncertainty in k_{exch} is 3% (2σ).

A total of 26 evenly distributed light-emitting diodes (LEDs) with a central wavelength of around 370 nm and a width (full-width at half-maximum) of 13 nm were used to provide a homogeneous light flux through the chamber. The LEDs have the advantage over *e.g.* black-lamps that they result in less heating of the chamber and thus less desorption of organic nitrates adsorbed on the chamber walls, which could complicate

the analysis of *e.g.* decays rates due to photolysis. An emission spectrum of the LEDs is given in the Results section.

2.2. HR-ToF-ICIMS

Measurements of organic nitrates, organic acids, alcohols and N_2O_5 were conducted with a high-resolution time-of-flight Iodide-chemical-ionization mass spectrometer (HR-ToF-ICIMS, Lee *et al.*,[37] Aerodyne Research Inc, USA) with a resolution of 5000 at *m/z* 250. The primary iodide ions were generated from photoionization of 40 parts-per-million CH_3I by volume (hereafter ppmv) in a flow of 1.0 L (STD) min^{-1} (hereafter SLM) N_2[38,39] before entering the ion–molecule-reactor, which was kept at 60 °C and 170 mbar. The HR-ToF-ICIMS sampled a total flow of 2.1 SLM into the ion–molecule reactor with 25% originating from the SCHARK. The remaining 75% was purified air, 10% of which was humidified to ~100% relative humidity at room temperature to maintain I^- and $I{\cdot}H_2O^-$ reagent ions at a constant level and ratio. During data processing, ions were identified using Tofware V4.0.3 (Aerodyne Research Inc.). HR-ToF-ICIMS signals were normalized to the total reagent ion signal, corrected for inlet flow dilution, and baseline-subtracted to yield normalized counts per second (ncps). The limit of detection (LOD) was determined as three times the standard deviation (3σ) interval of the respective ion signal during zero-air measurement. In order to focus on the major products, only ions with signal intensities exceeding three times the LOD were included in the analysis. The HR-ToF-ICIMS was calibrated for N_2O_5 by comparison with a thermal-dissociation cavity-ringdown-spectrometer (TD-CRDS).[39] No calibration standards are available for the limonene derived organic nitrates measured here; however, total multifunctional organic nitrates were also quantified using a TD-CRDS as described below. An average detection sensitivity of the HR-ToF-ICIMS for the organic nitrates is reported in Section 3.1.

2.3. Five-channel cavity ring-down spectrometer

A five-channel cavity ring-down spectrometer[40] was used to measure NO_2, NO_x, $\sum$PNs (peroxy nitrates, RO_2NO_2) and $\sum$ANs (multifunctional (''alkyl'') nitrates, $RONO_2$). The ''blue-channels'' of the instrument used laser diodes emitting at 409 nm where NO_2 absorbs. NO_2 was measured directly after sampling through an unheated inlet whereas $\sum$PNs and $\sum$ANs were thermally dissociated to NO_2 by heating their separate PFA and Quartz inlets[36] to 448 and 648 K, respectively. The five-channel cavity ring-down spectrometer was operated in NO_x rather than NO_2 mode to minimize bias from secondary reactions when measuring $\sum$ANs and $\sum$PNs following thermal dissociation.[35]

The cavity ring-down spectrometer was connected to the SCHARK *via* ~160 cm of $\frac{1}{4}$-inch (0.635 cm ID) PFA tubing. Sample air entered each cavity at a flow rate of 2.1 SLM. Zeroing of the instrument was performed by overfilling the inlet line with dry zero air. Ring-down times were converted to mixing ratios using the effective absorption cross section σ_λ of NO_2 at 409 nm. The value of σ_λ was calculated from the overlap between the laser emission and the NO_2 absorption spectrum.[41] The laser emission spectrum was recorded with a dedicated CCD spectrometer (Ocean Optics HR4000). The effective cross section was typically within a few percent of 6.4×10^{-19} cm^2 $molecule^{-1}$.

The LOD for NO_x and $\sum$ANs was determined by measuring zero air over a period of one hour. The 2σ standard deviation for NO_x and $\sum$ANs are 40 and 30 pptv, respectively (for an integration time of 1 s). Using these values the detection limits for NO_x and $\sum$ANs are 40 and 50 pptv, respectively. Note that the LOD for $\sum$ANs is obtained by error propagation in both the NO_x and $\sum$ANs channels. The total uncertainty of the NO_x measurements includes the uncertainty associated with the absorption cross section[41] and fluctuations in the laser emission spectrum, which together amount to 6.5%.[42] The total uncertainty associated with the $\sum$ANs measurements depends on the total uncertainty of the NO_x channel and amount to ~9%. Mixing ratios attributed to $\sum$PNs were below the detection limit under our experimental conditions and are therefore not discussed further in this study.

2.4. Experimental procedure

Limonene nitrates were formed by the reaction of limonene with NO_3 in dry air in the SCHARK chamber. NO_3 was generated by thermal decomposition of N_2O_5, which was introduced into the chamber by passing ~500 cm^3 (STD) min^{-1} (hereafter sccm) dry zero air over N_2O_5 crystals held at 195 K (dry ice acetone bath). N_2O_5 was synthesized by flowing 150 sccm of NO (5% in N_2, Westfalen) and 200 sccm of O_2 with ~4% O_3 (generated *via* electrical discharge) through a 2 L glass reaction vessel.[43] The resulting N_2O_5 was trapped as colourless crystals in a glass vessel held at 195 K. The N_2O_5 crystals were stored at 243 K until use (for a maximum of 2 days). This source of NO_3 was preferred to the *in situ* reaction between NO_2 and O_3 as the latter also reacts with limonene. Limonene was introduced into the chamber *via* flow-controllers connected to a steel canister containing 430 ppmv limonene (96%, Sigma-Aldrich) in He (5.0, Westfalen). O_3 was continuously monitored during the photolysis experiments using a commercial UV absorption instrument (2B Technologies Model 205), operating at 254 nm. The LOD of the O_3 monitor was 2 ppbv for a 10 s averaging time.

Each experiment had a duration of between 3 and 5 hours, after which the SCHARK chamber was cleaned by flushing first with humidified zero air (for 1–2 hours) to remove residual reactive nitrogen species, followed by dry zero air (overnight) to remove remaining humidity.

3. Results and discussion

3.1. Formation of limonene-nitrates (LIM-ONO_2)

Fig. 1 shows the results of an experiment in which a flow of 2.8 sccm limonene ($C_{10}H_{16}$) in air (430 ppmv) in a total flow of 12.5 SLM zero-air was introduced into the chamber (prefilled with zero-air), resulting (after ~20 min) in a limonene concentration of ~20 ppbv. This was followed by three injections of N_2O_5 (at 08:07, 08:42 and 09:56) initiating the formation of various LIM-ONO_2 that were detected using HR-ToF-ICIMS

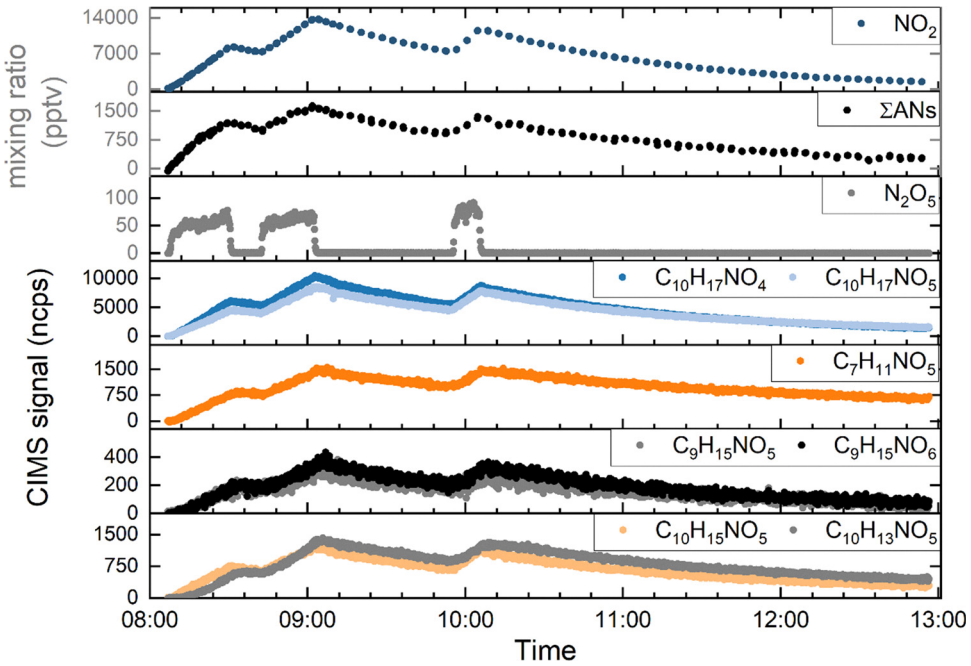

Fig. 1 Time series of mixing ratios of N_2O_5 and selected LIM-ONO_2 formed in the reaction between NO_3 and limonene in air as detected by HR-ToF-ICIMS. The NO_2 and ∑ANs measurements were made using the TD-CRDS. Limonene was initially present at 20 ppbv with three additions of N_2O_5 (08:07 to 08:30, 08:42 to 09:04 and 09:56 to 10:06).

(lower 4 panels in Fig. 1). The mixing ratio of N_2O_5 that was injected was approximately 16 ppb, derived by numerical simulation of the measured mixing ratios in the SCHARK (Fig. S1).

With one exception ($C_7H_{11}NO_5$), the strongest signal intensities (molecules in bold in the following text) observed were from C10 nitrates clustered with iodide. These were observed at *m/z* 342.02 (**$C_{10}H_{17}NO_4$**), 358.02 (**$C_{10}H_{17}NO_5$**), (**$C_{10}H_{15}NO_5$**) and 353.98 (**$C_{10}H_{13}NO_5$**). Weaker signals were observed from $C_{10}H_{15}NO_6$, $C_{10}H_{15}NO_7$, $C_{10}H_{16}N_2O_6$ and $C_{10}H_{17}NO_6$.

In addition to C10 nitrates we also observed $C_2H_4N_2O_6$, $C_2H_5NO_4$, $C_3H_5NO_4$, $C_3H_5NO_5$, $C_4H_7NO_5$, $C_4H_8N_2O_6$, $C_4H_9NO_4$, $C_6H_9NO_5$, $C_6H_{12}N_2O_6$, $C_7H_9NO_6$, **$C_7H_{11}NO_5$**, $C_7H_{11}NO_6$, $C_8H_{13}NO_5$, $C_8H_{13}NO_6$, $C_8H_{15}NO_4$, $C_9H_{13}NO_6$, $C_9H_{13}NO_7$, **$C_9H_{15}NO_5$**, **$C_9H_{15}NO_6$**. The *m/z* ratios, relative signal intensities and saturation mass concentration for all nitrates detected are listed in Table S1 and displayed in Fig. S2 which segregate the nitrates into low, semi and intermediate volatility VOCs (LVOC, SVOC and IVOC, respectively).[44,45] The high abundance of IVOC compared to LVOC indicates that significant aging and partitioning into the particle phase has not occurred in our experiments. In Fig. 1 we plot the signal intensities for seven organic nitrates (those in bold-type above), selected either for their large signal intensities or because they are expected to be the main products of the reaction. The total multifunctional alkyl nitrate mixing ratio (ΣANs) as determined from the TD-CRDS measurement reached a maximum of 1.7 ppbv (at ~09:00), coincident with the maximum HR-ToF-ICIMS signals and maximum NO_2 mixing ratio (13 ppbv). With the exception of N_2O_5, the mixing ratios/signals of the trace-gases shown in Fig. 1 exhibit similar trends in production (as long as N_2O_5 is present) and loss (due to flow-out of the SCHARK) when N_2O_5 has depleted to zero. The time scale (~60–90 s) for N_2O_5 to disappear after its flow into the SCHARK was ceased is commensurate with its thermal decomposition rate coefficient at 1 bar and 298 K (4.4×10^{-2} s^{-1}) and the fact that each NO_3 formed is rapidly scavenged (within 0.2 s) by limonene (20 ppbv).

Fig. 2 shows the time-dependent contributions of the 4 dominant organic nitrates to the total signal, with the remaining signals summed and shown in grey. The relative composition does not change significantly with the number of N_2O_5 additions. The pie-chart inset indicates the contributions of each LIM-ONO_2 signal at 10:07 after the three N_2O_5 injections. Note that the data are based on the HR-ToF-ICIMS signal intensities rather than mixing ratios of each nitrate during the gas-phase sampling period and the actual composition could be different. The largest signal is associated with $C_{10}H_{17}NO_4$ which accounts for 38.5% of the total LIM-ONO_2 signal. This is followed by $C_{10}H_{17}NO_5$ (28.5%), $C_7H_{11}NO_5$ (5%) and $C_{10}H_{15}NO_5$ (4.6%). The remaining 22 nitrate species each contribute less than 4.5%, but together account for 23.1% of the total signal. No significant experiment-to-experiment variation in the fractional contribution of the 4 main organic nitrates was observed.

Table 1 lists the LIM-ONO_2 species identified by the HR-ToF-ICIMS and indicates which ones could be cold-trapped and re-injected into the SCHARK before subject to photolysis. The likely functional groups are those previously reported in the literature (where available). While the exact structures remain uncertain, the LIM-ONO_2 are likely formed *via* RO_2 + RO_2

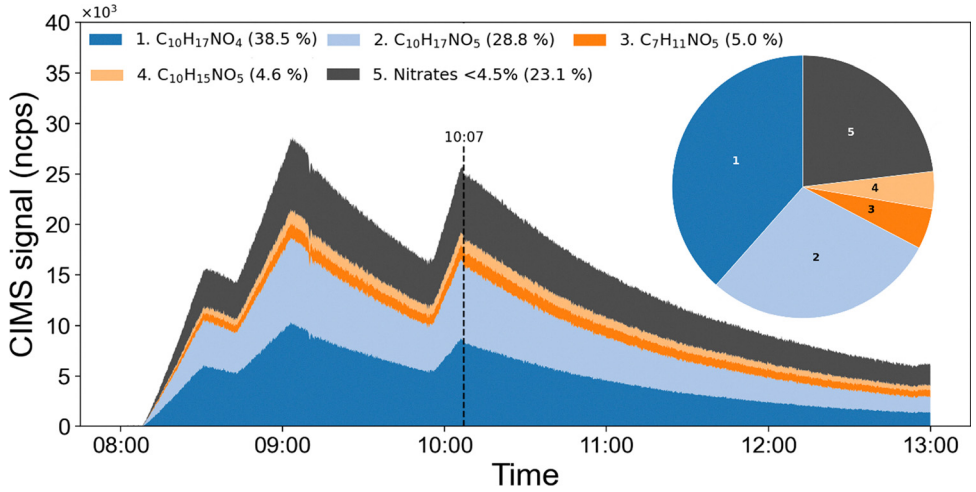

Fig. 2 Time-dependent stack plot of the LIM-ONO_2 composition (based on HR-ToF-ICIMS measurements) formed in the SCHARK during the NO_3-initiated oxidation of limonene. The pie chart shows the relative contribution of the LIM-ONO_2 species after three N_2O_5 injections (at 10:07) under the assumption that all LIM-ONO2 species have the same ionization efficiencies for association with I^-.

Table 1 LIM-ONO_2 detected during the NO_3 initiated oxidation of limonene

LIM-ONO_2	Functional groups (excluding nitrate)	Ref.	Trapping behaviour	Photolysis behaviour	J (10^{-4} s^{-1})
$C_{10}H_{17}NO_4$	Hydroxy (Fig. S3)	Mayorga *et al.*[25] Ayres *et al.*[46] Devault *et al.*[22] Fry *et al.*[19]	Always	–	1.69 ± 0.06 5.32 ± 0.07[a]
$C_{10}H_{17}NO_5$	Hydroperoxy/carbonyl, hydroxy (Fig. S3)	Ayres *et al.*[46] Mayorga *et al.*[25] Devault *et al.*[22]	Sometimes	+	—
$C_7H_{11}NO_5$	Hydroxy, carbonyl	Takeuchi *et al.*[47]	Sometimes	+	—
$C_{10}H_{15}NO_5$	Dicarbonyl (Fig. S3)	Devault *et al.*[22] Ayres *et al.*[46]	Always	–	—
$C_{10}H_{13}NO_5$		—	Always	–	—
$C_{10}H_{15}NO_6$		Faxon *et al.*[24]	Always	+	—
$C_{10}H_{15}NO_7$		Takeuchi *et al.*[47]	Sometimes	+	—
$C_9H_{15}NO_5$	Carbonyl, hydroxy (see Fig. S3)	Faxon *et al.*[24] Mayorga *et al.*[25] Fry *et al.*[19]	Never	+	—
$C_9H_{15}NO_6$		Mayorga *et al.*[25]	Never	+	—
$C_9H_{13}NO_6$		Mayorga *et al.*[25]	Never	+	—
$C_9H_{13}NO_5$		Mayorga *et al.*[25]	Never	+	—
$C_{10}H_{17}NO_6$	Dicarbonyl, hydroxy (see Fig. S3)	Mayorga *et al.*[25] Fry *et al.*[19] Faxon *et al.*[24]	Never	+	—
$C_{10}H_{16}N_2O_6$	Dinitrate	—	Always	–	1.22 ± 0.06

Notes: Faxon *et al.*,[24] Takeuchi *et al.*[47] and Fry *et al.*[19] reported particle-phase measurements. Additionally Fry *et al.*[19] proposed a gas phase mechanism. + indicates an increase in the CIMS signal, – indicates a decrease in the CIMS signal. [a] indicates that the measured photolysis frequency was determined in the absence of cyclohexane.

reactions, since the high limonene concentration in the chamber suppresses reactions of RO_2 with NO_3. A simple numerical simulation indicates that, under high limonene conditions in the chamber, product formation from RO_2 + RO_2 reactions exceeds that from RO_2 + NO_3 reactions by a factor of ~200 (Fig. S1). The proposed gas-phase mechanisms leading to the formation of some of the LIM-ONO_2 species observed are shown in Fig. S3.

The main LIM-ONO_2 species ($C_{10}H_{17}NO_4$, $C_{10}H_{17}NO_5$, $C_7H_{11}NO_5$ and $C_{10}H_{15}NO_5$) observed in our experiments are consistent with previous reports. Devault *et al.*[22] identified $C_{10}H_{17}NO_4$ and $C_{10}H_{17}NO_5$ as the most intense contributors in the I-CIMS mass spectra, with additional detection of $C_{10}H_{15}NO_5$. Mayorga *et al.*[25] reported signals corresponding to $C_{10}H_{15,17}NO_{4,5}$ and $C_9H_{13,15}NO_{5\text{-}8}$ in both gas and particle phases, indicating that $C_{10}H_{15,17}NO_{4,5}$ are likely first-generation products. Takeuchi *et al.*[47] identified $C_7H_{11}NO_5$ as a characteristic product in thermal desorption particle-phase analysis. HR-ToF-ICIMS measurements (Faxon *et al.*[24]) report dominant SOA species including $C_{10}H_{15}NO_6$, $C_{10}H_{17}NO_6$ and $C_9H_{13}NO_7$.

Fig. 3 shows a correlation between the total multifunctional alkyl nitrates (in pptv) measured by TD-CRDS and the summed

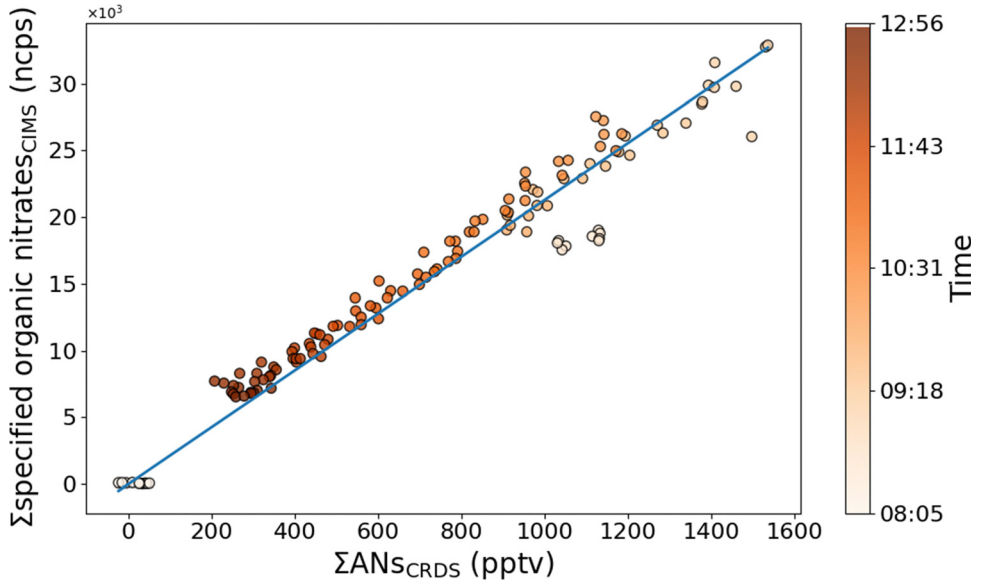

Fig. 3 Correlation between total alkyl nitrates measured by TD-CRDS and summed, nitrogen-weighted organic nitrates signal detected by HR-ToF-ICIMS during the formation of LIM-ONO_2. The blue line represents the result of an unweighted, least-squares regression to the data forced through the origin with a slope of (21.22 ± 0.14) ncps $pptv^{-1}$ (r = 0.99). The spread in CRDS data close to "zero" mixing ratios reflect fluctuations in zero measured before the first injection of N_2O_5 and is similar to the LOD for this device. Only data are included during which N_2O_5 was completely depleted.

HR-ToF-ICIMS signals (in normalised counts per second, ncps) of the individual organic nitrates in the absence of N_2O_5. The HR-ToF-ICIMS signals were multiplied by a factor 1 or 2 according to the number of nitrogen atoms in each species. A linear regression (blue line) was performed on the data obtained when N_2O_5 was absent (N_2O_5 can also be detected with the TD-CRDS at the TD-temperature for organic nitrates (648 K) and may therefore introduce artefacts in the data).

Assuming equal sensitivity of the HR-ToF-ICIMS to all detected LIM-ONO_2, the regression slope provides an estimate of the HR-ToF-ICIMS sensitivity of 21 ncps $pptv^{-1}$. An absolute sensitivity comparison to other CIMS instruments is hampered by various technical and operational factors.[48,49] Therefore, a relative comparison with the sensitivity of commonly calibrated species for this CIMS appears to be most appropriate. A sensitivity of 21 ncps $pptv^{-1}$ is broadly consistent with that observed for iodide clusters from N_2O_5 (~30 ncps $pptv^{-1}$) under identical operational conditions.[39] As N_2O_5 is detected (as an iodide-cluster) with high sensitivity by HR-ToF-ICIMS, we conclude that reaction of I^- with LIM-ONO_2 (to form iodide-clusters) occurs at a similar rate coefficient.

3.2. LIM-ONO_2 extraction/isolation

In order to extract and isolate LIM-ONO_2 formed as described above, a flow of 5 SLM from the chamber was passed through a glass spiral (Fig. S4) submerged in a cooling liquid at −30 °C. To avoid further reaction in the condensed phase, the sampling was conducted only in periods when N_2O_5 (and thus NO_3) was completely depleted. Between experiments, the glass spiral was cleaned with distilled water, followed by drying at 100 °C. Typically, LIM-ONO_2 were collected over a period of ~3 hours in this manner and subsequently stored in the glass-spiral at −78 °C (acetone/dry ice mixture) overnight, during which the SCHARK was flushed with humidified zero air in preparation for the next day's experiments.

Fig. 4a shows the time-series signals of three specific LIM-ONO_2 ($C_{10}H_{17}NO_4$, $C_{10}H_{15}NO_5$, $C_{10}H_{13}NO_5$) measured by the HR-ToF-ICIMS during an experiment in which N_2O_5 had been injected to form LIM-ONO_2 and products was sampled (after N_2O_5 had decayed to zero) *via* the glass-spiral at either room temperature (09:20 to 09:26 and 09:32 to 09:40) or when the glass-spiral was cooled to −30 °C (shaded grey). Note that (according to CPC measurements) no particles were present in the SCHARK during sampling into the cold trap.

The almost complete loss of the $C_{10}H_{17}NO_4$ signal when sampling through the spiral at −30 °C indicates efficient trapping of these LIM-ONO_2. In contrast, experiments using a GC-MS[50] revealed that, at −30 °C, limonene was not trapped in the glass spiral to a significant extent at the typical mixing ratios used for the SCHARK experiments.

The fact that the LIM-ONO_2 signals did not immediately go to zero when the glass-spiral was cooled, reflects the fact that we are dealing with molecules that have a high surface affinity (as would be expected for trace gases with large molecular weight and a high degree of substitution by polar groups) and that some desorption from the PFA-tubing between the glass-spiral and the HR-ToF-ICIMS takes place. The three different time-series of $C_{10}H_{17}NO_4$, $C_{10}H_{15}NO_5$ and $C_{10}H_{13}NO_5$ indicate that they have different affinities for the tubing between the glass-spiral and the HR-ToF-ICIMS, with $C_{10}H_{17}NO_4$ (hydroxy-nitrate, blue) being less "sticky" (*i.e.* the signal decays more rapidly) than $C_{10}H_{15}NO_5$ (di-carbonyl-nitrate, orange) and $C_{10}H_{13}NO_5$ (dark grey).

The temperature dependent desorption of LIM-ONO_2 from the glass spiral was examined by passing a flow of 200 sccm

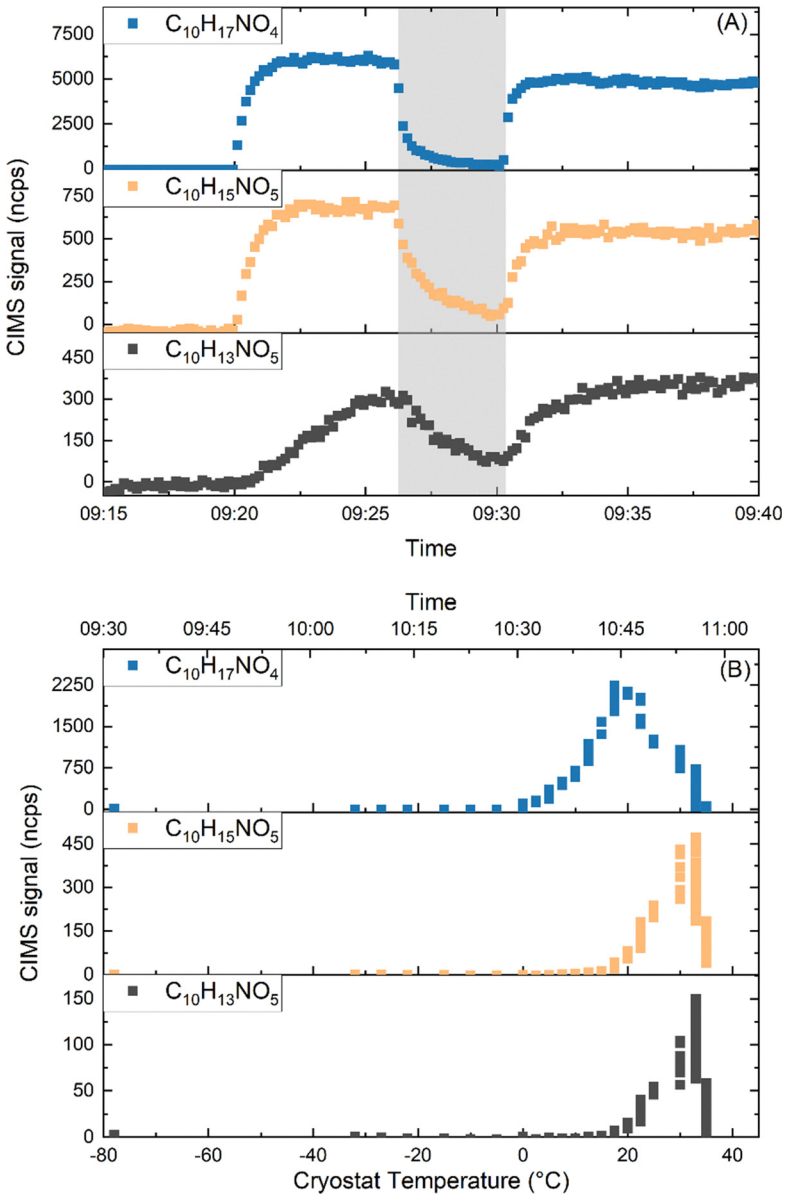

Fig. 4 (A) HR-ToF-ICIMS time series for $C_{10}H_{17}NO_4$, $C_{10}H_{15}NO_5$ and $C_{10}H_{13}NO_5$ while sampling from the SCHARK through a glass-spiral held at either room temperature or −30 °C (grey shaded area). (B) Desorption of trapped $C_{10}H_{17}NO_4$, $C_{10}H_{15}NO_5$ and $C_{10}H_{13}NO_5$ from the glass-spiral while warming from −78 °C (overnight storage temperature) to 35 °C with a continuous flow of zero-air (200 sccm).

zero-air through the glass-spiral prior to further dilution (5–10 SLM) and transport (*via* ∼2 m of PFA tubing) to the HR-ToF-ICIMS (*i.e.* bypassing the SCHARK). Fig. 4b shows the results obtained when the glass-spiral was continuously warmed from −78 °C to 35 °C over a period of ∼80 minutes. The first LIM-ONO_2 to start desorbing was $C_{10}H_{17}NO_4$ at a temperature of ∼0 °C with the maximum signal at 20 °C after which the signal decreased. A single (albeit broad) desorption feature is observed, indicating that the physical adsorption of $C_{10}H_{17}NO_4$ on the glass-surface is limited to one type of site or that multiple adsorption sites have similar binding energies. Desorption of both $C_{10}H_{15}NO_5$ and $C_{10}H_{13}NO_5$ started at a temperature of ∼15 °C with the maximum signals obtained at 30 and 35 °C, respectively. As expected, the nitrates requiring higher temperatures to desorb from the glass surface are those that displayed the slowest decrease in Fig. 4a. This result is intuitive and related to the vapour pressure of the LIM-ONO_2 and their affinity for surfaces. Similar plots illustrating the adsorption (trapping) and desorption of the other LIM-ONO_2 are shown in Fig. S5 and S6. In Fig. S5 we see that the signals of nearly all the C10 LIM-ONO_2 decrease when the sample is passed through the glass-spiral at −30 °C. Exceptions to this are $C_{10}H_{17}NO_6$ and $C_9H_{15}NO_5$ whose signals clearly increases during the trapping phase. As trapping only took place after N_2O_5 and NO_3 were consumed, it is unlikely that these signals arise through condensed-phase chemistry involving NO_3 or N_2O_5. However, we cannot rule out that the co-condensation of HNO_3 in the trap (Fig. S6c) may have led to some chemical

reactions in which *e.g.* $C_{10}H_{17}NO_6$, and $C_9H_{15}NO_5$ are formed. We also note that several C3 nitrates (*e.g.* $C_3H_5NO_4$, $C_3H_5NO_5$) and a C4-dinitrate ($C_4H_8N_2O_8$) were also trapped at −30 °C. The trapping behaviour of the most abundant limonene nitrates are summarized in Table 1. Trapping behaviour designated "always" means that the species could be effectively trapped in the glass-spiral, stored overnight (while the SCHARK was flushed) and transferred into the chamber by rapidly warming with warm water at ∼40–50 °C while passing 500 sccm of zero air through the glass-spiral in all experiments. Trapping behaviour designated "sometimes" means that we could trap the molecules in some of the experiments but not in all and "never" means that this LIM-ONO_2 was not trapped. We have no definite explanation for the lack of reproducibility, which may be related to changes in composition of the mixture and effects related to competitive adsorption on the cold glass-surface.

3.3. Interaction of LIM-ONO_2 with chamber walls in the SCHARK

As LIM-ONO_2 compounds have a high affinity for surfaces, we expect that some fraction is lost to the walls of the SCHARK chamber. Such effects must be corrected for when deriving *e.g.* production rates through NO_3 + limonene chemistry or loss rates due *e.g.* due photolysis. The ability to trap LIM-ONO_2 and re-inject them into a clean chamber in which the production rate is zero, allows us to check for the wall losses of each individual LIM-ONO_2.

Wall loss rate coefficients (k_{wall}) for LIM-ONO_2 were quantified by injecting LIM-ONO_2 from the glass-spiral into the SCHARK and monitoring their concentration decrease over time in the dark and in the absence of oxidants (*e.g.* O_3 or NO_3). Time dependent LIM-ONO_2 signals measured by the HR-ToF-ICIMS decayed exponentially and the time series was fitted to a first-order expression (eqn (1)) to derive the species-specific wall-loss rate constant k_{wall}.

$$[\text{LIM-ONO}_2]_t = [\text{LIM-ONO}_2]_0 \times \exp - (k_{wall} + k_{exch})\, t \qquad (1)$$

where $[\text{LIM-ONO}_2]_0$ and $[\text{LIM-ONO}_2]_t$ are the LIM-ONO_2 signals directly after the addition and after t seconds, respectively and k_{exch} (1.09×0^{-4} s^{-1}) accounts for flow out of the chamber. Note that this expression assumes no sources of LIM-ONO_2 (*i.e.* desorption from the walls).

For $C_{10}H_{17}NO_4$ (Fig. 5, lower panel) the observed exponential decay constant in the $C_{10}H_{17}NO_4$ signal is similar to k_{exch} (solid black line), indicating that this compound does not exhibit a measurable wall loss within the uncertainty of the experiment. The behaviour of $C_{10}H_{17}NO_5$ is markedly different: the observed decay constant (k_{wall} + k_{exch}) is significantly smaller than the exchange rate. In the absence of chemical production of $C_{10}H_{17}NO_5$ this can only be explained in terms of multi-phase equilibria, in which $C_{10}H_{17}NO_5$ that has been adsorbed to the wall during the injection phase (*i.e.* before t = 0) desorbs back into the gas-phase, thereby reducing its overall decay rate. Close inspection of the signal during injection reveals a sharp decrease in signal as soon as the injection stops (*e.g.* from 700 to 460 ncps for $C_{10}H_{17}NO_5$). This is not a mixing effect but clear evidence for uptake of the LIM-ONO_2 to the chamber walls. For $C_{10}H_{17}NO_4$ (lower panel of Fig. 5) the initial, fractional decrease after injection stops is smaller and the loss rate no longer significantly different from k_{exch}. Fig. S7 shows that none of the major LIM-ONO_2 species are totally free from wall effects as the decay rates are often lower than k_{exch}. The LIM-ONO_2 with the largest signal ($C_{10}H_{17}NO_4$) shows a relatively small initial decrease in signal

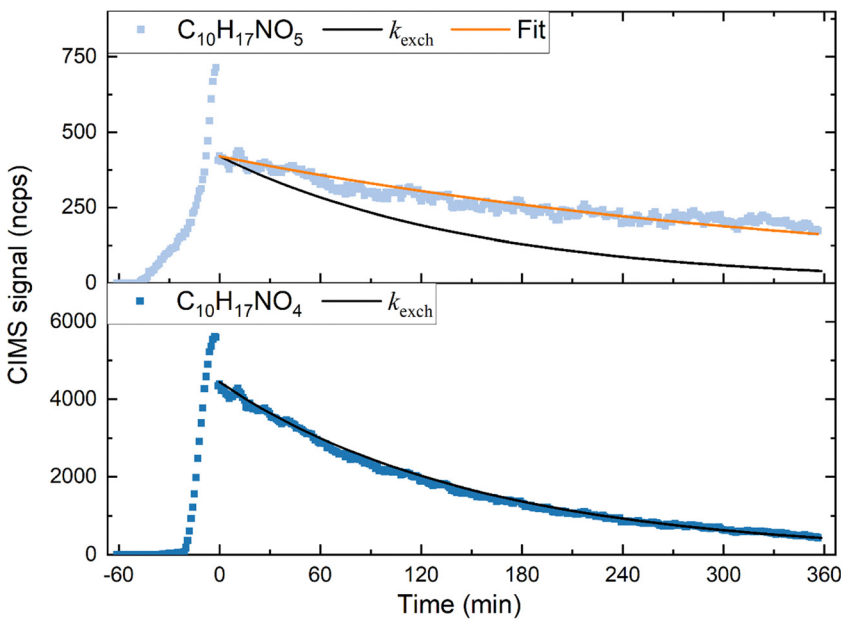

Fig. 5 LIM-ONO_2 signal ($C_{10}H_{17}NO_4$ and $C_{10}H_{17}NO_5$) in SCHARK. The black lines are calculated from the exchange rate constant k_{exch}. The orange line is the first-order exponential fit to the data: the decay constant for $C_{10}H_{17}NO_5$ is 4.45×10^{-5} s^{-1}. Negative times correspond to the period prior to and during the injection of LIM-ONO_2.

after injection into the "clean" SCHARK and its long-term behaviour is consistent with a trace gas whose only loss is due to flow out of the chamber. For these reasons, we now focus our analysis on $C_{10}H_{17}NO_4$ for which auxiliary data such as absorption cross sections are available (see below).

3.4. Photolysis and lifetime of the dominant LIM-ONO_2 ($C_{10}H_{17}NO_4$)

To investigate the behaviour of the various LIM-ONO_2 species under irradiation (at a wavelength of 370 ± 13 nm), a cold-trapped sample was transferred from the glass-spiral into the SCHARK by warming rapidly using a water-bath at ~40–50 °C while passing 500 sccm of zero air through the glass-spiral (see Section 3.2). To examine the potential formation of OH and assess its contribution to the overall loss of LIM-ONO_2 during photolysis, experiments were carried out either with or without cyclohexane (120 ppmv) that serves as a OH scavenger.

The time profiles for the measured signal intensity for $C_{10}H_{17}NO_4$ under irradiation (from experiments both with and without added cyclohexane) are displayed in Fig. 6 (left y-axis). Following a short period (2 min) after injection of LIM-ONO_2 to allow for mixing in the SCHARK, the LEDs were switched on to irradiate the gas-mixture. During irradiation, the NO_2 mixing ratio increases as expected if the main process in LIM-ONO_2 photolysis is cleavage of the O–NO_2 bond. Note however, that NO_2 is rapidly photolysed using the LEDs (J_{NO_2} = 14.0 × 10^{-3} s^{-1}) to form O(^{3}P) and thus O_3. No increase in the O_3 concentration was observed, which is related to the 2 ppbv detection limit of the ozone-monitor. In addition, the NO_2 formed also react with peroxy radicals generated during

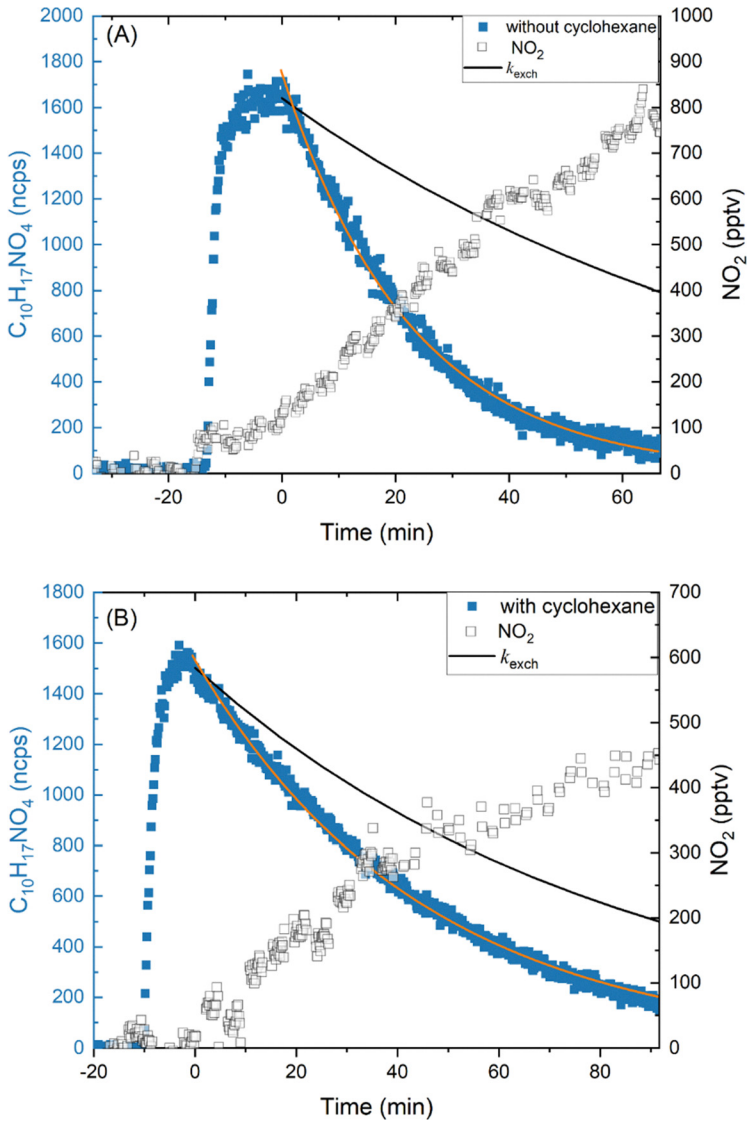

Fig. 6 Time-dependent signals of $C_{10}H_{17}NO_4$ during a photolysis experiment with (B) and without (A) cyclohexane as OH scavenger. The LEDs were switched on at Time = 0 min. The black lines are calculated from the exchange rate constant k_{exch}. The orange lines show the first-order exponential fit to the data during photolysis. The decay constants were 7.32 × 10^{-4} s^{-1} (without cyclohexane) and 3.69 × 10^{-4} s^{-1} (with cyclohexane) The measured NO_2 is shown on the right y-axis.

photolysis (and also from OH scavenging by cyclohexane) to form *e.g.* peroxy nitrates which will sequester some of the NO_x. For this reason, the NO_2 profile cannot be analysed to calculate *e.g.* the relative importance of O–NO_2 bond fission in comparison to formation of other photochemical fragments.

A control experiment confirmed that no detectable nitrate-containing products were produced or released from the chamber walls when the LEDs were switched on without prior injection of LIM-ONO_2 from the glass-spiral.

In the presence of cyclohexane, the overall loss of $C_{10}H_{17}NO_4$ is by photolysis, flow out of the chamber and wall loss and is given by:

$$[C_{10}H_{17}NO_4]_t = [C_{10}H_{17}NO_4]_0 \times \exp - (J_{C_{10}H_{17}NO_4} + k_{wall} + k_{exch})\, t \quad (2)$$

This expression does not consider loss processes for $C_{10}H_{17}NO_4$ through reaction with other trace gases. A potential exception to this is the reaction with O_3. Although O_3 is not present in the initial mixture injected into the SCHARK prior to photolysis, it will be generated *via* the photolysis of the primary photo-product NO_2. The amount of O_3 that can be generated per LIM-ONO_2 photolysed is a complex function of the recycling of NO *via* reactions with peroxy radicals:

$$\text{LIM-ONO}_2 + h\nu \rightarrow \text{LIM-O} + \text{NO}_2 \quad (R4)$$

$$\text{NO}_2 + h\nu \rightarrow \text{NO} + \text{O}(^3\text{P}) \quad (R5)$$

$$\text{O}(^3\text{P}) + \text{O}_2 + \text{M} \rightarrow \text{O}_3 + \text{M} \quad (R6)$$

$$\text{LIM-O} + \text{O}_2 \rightarrow \text{RO}_2 \quad (R7)$$

$$\text{RO}_2 + \text{NO} \rightarrow \text{LIM-O} + \text{NO}_2 \quad (R8)$$

$$\text{LIM-ONO}_2 + \text{O}_3 \rightarrow \text{products} \quad (R9)$$

Where LIM-O is the alkoxy radical formed when the O–NO_2 bond breaks during photolysis. The rate coefficient for reaction of LIM-ONO_2 with O_3 has been reported to be 1.7×10^{-17} cm^3 $molecule^{-1}$ s^{-1}.[31] It would thus require the presence of ~40 ppb O_3 to induce a positive bias of 10% in our loss term for $C_{10}H_{17}NO_4$. As we observed <2 ppbv O_3 (the LOD of the ozone monitor) we conclude that neglecting the reaction between photochemically generated O_3 and $C_{10}H_{17}NO_4$ in the further analysis is justified.

For $C_{10}H_{17}NO_4$, the slope of the regression from the experiment with added cyclohexane ($J_{C_{10}H_{17}NO_4} + k_{wall} + k_{exch}$) was 3.69×10^{-4} s^{-1}. Using the chamber exchange constant for the flow conditions of this experiment ($k_{exch} = 2.00 \times 10^{-4}$ s^{-1}) and the fact that no significant wall loss was observed ($k_{wall} + k_{exch} \approx k_{exch}$, see above) we derive $J_{C_{10}H_{17}NO_4} = (1.69 \pm 0.06) \times 10^{-4}$ s^{-1}.

In the absence of cyclohexane, $C_{10}H_{17}NO_4$ was lost much more rapidly due to reaction with photochemically formed OH. The loss frequency (after subtracting k_{exch}) was 5.32 ($\pm$0.07) $\times$ 10^{-4} s^{-1}. This indicates that a large fraction (0.75) of $C_{10}H_{17}NO_4$ was lost *via* reaction with OH when cyclohexane was not added. A likely source of OH during irradiation is the photolysis of HONO which absorbs strongly at wavelengths of λ = 360–370 nm and has a SCHARK photolysis frequency of $J_{HONO} = 3.5 \times 10^{-3}$ s^{-1}. HONO was indeed detected (but not quantified) by HR-ToF-ICIMS and is presumably formed from the interaction of NO_2 with the chamber surface as has often been documented for Teflon environmental chambers.[51]

The photolysis frequency of $C_{10}H_{17}NO_4$ ($J_{C_{10}H_{17}NO_4}$) is a function of the photon flux through the SCHARK chamber, the absorption cross sections of $C_{10}H_{17}NO_4$ over the LED emission spectrum ($\lambda = 370 \pm 13$ nm), and the photodissociation quantum yield (ϕ) at these wavelengths. To put our observed loss frequency on a physical basis we performed chemical actinometry using Cl_2 which absorbs at $\lambda = 370 \pm 13$ nm with known cross sections and quantum yields.

$$[Cl_2]_t = [Cl_2]_0 \times \exp - (J_{Cl_2} + k_{exch})\, t \quad (3)$$

The relative loss rate of $C_{10}H_{17}NO_4$ and Cl_2 due to photolysis is given by:

$$\frac{d[C_{10}H_{17}NO_4]/dt}{d[Cl_2]/dt} \propto \frac{\sigma_{av}(C_{10}H_{17}NO_4)}{\sigma_{av}(Cl_2)} \cdot \frac{\phi_{av}(C_{10}H_{17}NO_4)}{\phi_{av}(Cl_2)} \cdot \frac{f_{C_{10}H_{17}NO_4}}{f_{Cl_2}} \quad (4)$$

where σ_i are average absorption cross sections weighted by wavelength dependent emission intensity of the LEDs, ϕ_i are primary photodissociation quantum yields and f_i are the photon flux during irradiation. As we are dealing with pseudo-first-order loss processes, the left-hand term can be modified to:

$$\frac{d[C_{10}H_{17}NO_4]/dt[C_{10}H_{17}NO_4]}{d[Cl_2]/dt[Cl_2]} \text{ or simply } \frac{J_{C_{10}H_{17}NO_4}}{J_{Cl_2}}$$

where J_i are photolysis frequencies (s^{-1}). As the same operating parameters and number of LEDs were used to photolyse both Cl_2 and $C_{10}H_{17}NO_4$, the last terms on the right-hand side of eqn (4) effectively cancel, so that the relative decay rate of Cl_2 and $C_{10}H_{17}NO_4$ is only related to physical constants of the molecules (σ and ϕ). For such experiments, Cl_2 represents an ideal actinometer as its absorption cross sections[52] and photodissociation quantum yield (unity) are well established.[18] However, it is important to avoid secondary chemistry including Cl_2 re-combination or loss *via* reaction with reactive species such as alkyl fragments. For these reasons, experiments to determine J_{Cl_2} were conducted in the presence of ~3 ppmv ethane, which reduces the Cl atom lifetime to ~0.2 ms and prevents recombination. The C_2H_5 radicals thus formed were quasi-instantaneously scavenged by O_2 (timescale of 30 ns for ~200 mbar [O_2]) to effectively prevent their reaction with Cl_2. The $C_2H_5O_2$ peroxy radicals formed do not react with Cl_2.

$$\text{Cl}_2 + h\nu \rightarrow 2\text{Cl} \quad (R10)$$

$$\text{Cl} + \text{C}_2\text{H}_6 \rightarrow \text{HCl} + \text{C}_2\text{H}_5 \quad (R11)$$

$$\text{C}_2\text{H}_5 + \text{O}_2 + \text{M} \rightarrow \text{C}_2\text{H}_5\text{O}_2 + \text{M} \quad (R12)$$

A mixture of 500 sccm Cl_2 (nominal 80 ppmv in N_2) and 10 SLM dry zero air was introduced in the chamber (for ~11 min), together with a single injection of ethane (6 mL of a 48% gas mixture in N_2). Resulting in initial mixing ratios of

~3 ppmv ethane (calculated from volumes and mixing ratio) and 290 ppbv Cl_2 (measured by CRDS).

After switching off the Cl_2 flow and waiting a few minutes for complete mixing, the LEDs were switched on and the Cl_2 mixing ratio decreased exponentially as shown in Fig. S8. In the absence of chemical losses other than photolysis, the Cl_2 loss is described by eqn (3). The sum ($J_{Cl_2} + k_{exch}$) was derived by fitting the data shown in Fig. S8 to expression (3). J_{Cl_2} was then obtained by subtracting the chamber exchange constant (1.82×10^{-4} s^{-1}), yielding an experimental, effective first-order photolysis frequency of $J_{Cl_2} = (1.99 \pm 0.01) \times 10^{-3}$ s^{-1}.

This is a factor ~11.8 larger than the value of $J_{C_{10}H_{17}NO_4} = (1.69 \pm 0.06) \times 10^{-4}$ s^{-1} obtained under quasi-identical conditions (*i.e.* f was unchanged).

At this point in the analysis, we have derived:

$$\frac{\sigma_{av}(C_{10}H_{17}NO_4)}{\sigma_{av}(Cl_2)} \cdot \frac{\phi_{av}(C_{10}H_{17}NO_4)}{\phi_{av}(Cl_2)} = \frac{1}{11.8} = 0.085 \quad (5)$$

$$(\text{for } \lambda = 370 \pm 13\,\text{nm})$$

If we now assume that the photodissociation quantum yield for $C_{10}H_{17}NO_4$ is unity at all wavelengths emitted by the LEDs (*i.e.* the same quantum yield as Cl_2) the 2nd term on the left-hand side of eqn (5) disappears. In this case, the value of 0.085 represents the ratio of the absorption cross sections of $C_{10}H_{17}NO_4$ and Cl_2 weighted over the LED emission spectrum. The Cl_2 absorption cross section averaged over the region of overlap with the LED emission is $\sigma_{av}(Cl_2) = 7.90 \times 10^{-20}$ cm^2 $molecule^{-1}$, which yields a weighted average absorption cross section for $C_{10}H_{17}NO_4$ over the same wavelength range (λ = 355–400 nm) of σ_{av} ($C_{10}H_{17}NO_4$) = 6.72×10^{-21} cm^2 $molecule^{-1}$.

This cross section can be compared to the spectrum of $C_{10}H_{17}NO_4$ reported by Wang *et al.*[31] (blue datapoints in Fig. 7), but with some caveats. Firstly, the spectrum reported by Wang *et al.*[31] was that of a sample dissolved in ether, which causes a solvatochromatic wavelength shift of unknown magnitude compared to the gas-phase. For this reason, Wang *et al.*[31] used ethyl ether as solvent because of its low polarity, which reduces the magnitude of the wavelength shift. Secondly, the spectrum of Wang *et al.*[31] covers the range λ = 200–367 nm and thus does not extend through the full range of wavelengths emitted by our LEDs (λ = 355–400 nm). To account for the second limitation, we have extrapolated the Wang *et al.*[31] spectrum to longer wavelengths assuming an exponential decrease in cross section with increasing wavelength. Here we also consider two different scenarios. In the first, (Extrapolation 1) we extend the observed exponential decrease in cross section observed by Wang *et al.*[31] between λ = 330 and 365 nm (dashed line in Fig. 7). As apparent from the log-plot, the discontinuation in the slope between 310 and 365 nm compared to shorter wavelengths may indicate a contribution from a different electronic transition. Alternatively, this could reflect a solvent effect or artefacts associated with low optical density and stray light at longer wavelengths. For this reason, in the second scenario (Extrapolation 2), we assume that the second feature in the absorption spectrum between ~λ = 310 and 365 nm is an artefact and we instead extend the exponential decrease in cross section between 260 and 310 nm to longer wavelengths. This behaviour is described by the solid blue line in Fig. 7 and leads to significantly lower cross sections at the longer wavelengths where our LEDs emit.

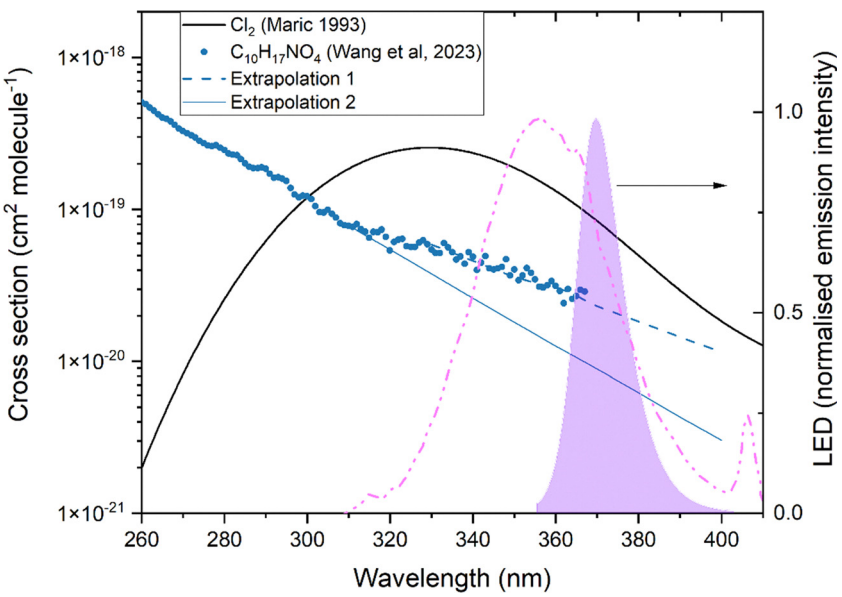

Fig. 7 Absorption spectra of Cl_2[52] and $C_{10}H_{17}NO_4$ (dissolved in ether) reported by Wang *et al.*[31] The solid and dashed lines are different extrapolations of the Wang *et al.* spectrum to longer wavelengths. The normalised LED emission spectra of the photolysis light sources used are also shown (right *y*-axis) with our LED emission spectrum the purple shaded area and the "black-lights" used by Wang *et al.* as a broken, purple line. The average cross-section, weighted by the LED emission spectrum in the same spectral region is either 2.27×10^{-20} cm^2 $molecule^{-1}$ (Extrapolation 1) or 8.57×10^{-21} cm^2 $molecule^{-1}$ (Extrapolation 2).

Using either scenario we can calculate the average cross section, weighted by the emission of our LEDs. Using scenario Extrapolation 1 (dotted line), we obtain σ_{av} (355–400 nm) = 2.27×10^{-20} cm^2 molecule^{-1}, whereas under scenario Extrapolation 2 the cross sections are reduced to σ_{av} (355–400 nm) = 8.57×10^{-21} cm^2 molecule^{-1}. The latter value is in reasonable agreement (within 25%) with that derived from our photolysis experiments and assuming that the quantum yield is unity ($\sigma = 6.72 \times 10^{-21}$ cm^2 molecule^{-1}).

Alternatively, by inserting the (extrapolated) average cross sections of Wang *et al.* into eqn (6) we can derive the effective quantum yield (ϕ_{av}) over this wavelength range. Under scenario Extrapolation 1, we obtain ϕ_{av} (355–400 nm) = 0.30 and under scenario Extrapolation 2 we obtain ϕ_{av} (355–400 nm) = 0.78 at 1 bar and 298 K. The quantum yield reported by Wang *et al.*[31] are much smaller with a value of 0.071 ± 0.035 and a chamber photolysis lifetime of $C_{10}H_{17}NO_4$ of 21 h. In contrast, we measured a chamber photolysis lifetime due to photodissociation of 1.6 h for $C_{10}H_{17}NO_4$.

In order to understand these differences in chamber lifetimes and derived quantum yields we first compare the emission spectra (normalised to λ_{max}) of the lamps used to photolyse limonene nitrates in both studies, which are plotted in Fig. 7. We see that the emission of the ''black-lights'' used by Wang *et al.* is broader (extending from ~320 to 400 nm) with a FWHM of ~40 nm and thus (compared to the LEDs) has more extensive overlap with the absorption spectrum of $C_{10}H_{17}NO_4$ at shorter wavelengths. As photodissociation quantum yields often *decrease* at longer wavelengths (lower photon energies) the difference in emission wavelengths cannot be the cause of the lower quantum yields observed by Wang *et al.* There are also large differences in the photon flux in both chambers. Wang *et al.*[31] report (in their SI) a photolysis frequency for NO_2 in their chamber of 2.1×10^{-3} s^{-1} which was obtained by photolysing NO_2 and modelling its loss (which is partially defined by reformation in the NO + O_3 reaction). We prefer to calculate J_{NO_2} from the accurately measured value of J_{Cl2} (1.99×10^{-3} s^{-1}) and the relative overlap of the LEDs with the well-known spectra of Cl_2 and NO_2 and associated quantum yields (both unity over the entire wavelength range of our LEDs). Our value of $J_{NO_2} = 14.0 \times 10^{-3}$ s^{-1} is a factor ~7 larger than that in the Wang *et al.* chamber and helps explain why we see almost complete loss of $C_{10}H_{17}NO_4$ within 80 min (Fig. 6) whereas Wang *et al.* observe a depletion of only 40% over a period of >4 hours (their Fig. 2), despite the better overlap between lamp emission and the UV absorption spectrum of $C_{10}H_{17}NO_4$.

A further explanation for the derivation of such different quantum yields is that we are actually dealing with different molecules of the formula $C_{10}H_{17}NO_4$ that are detected (in both Wang *et al.* and in this work) as clusters with I^-. Should this be the case, our analysis, which uses the (extrapolated) cross-sections from Wang *et al.* is inappropriate. As the $C_{10}H_{17}NO_4$ molecule in this work was generated in the reaction of NO_3 with limonene and not by wet-synthetic methods as in Wang *et al.*, we cannot rule this out. However, in the absence of a further analytical tool (*e.g.* gas chromatography) which to compare both samples, this remains purely speculative.

In summary, we observe that $C_{10}H_{17}NO_4$ is a photolabile organic nitrate formed in the NO_3-initiated oxidation of limonene, even when irradiated at the relatively long wavelengths emitted by our LEDs (λ = 355–400 nm) and that our data are compatible with a large quantum yield (possibly unity) if our extrapolation of the $C_{10}H_{17}NO_4$ spectrum reported by Wang *et al.*[31] is appropriate.

By convoluting the extrapolated $C_{10}H_{17}NO_4$ spectrum (Scenario: Extrap 2) with the solar spectral photon flux (measured on a cloud free day (23. July) at a Latitude of 35° and Longitude 32°) and a quantum yield of 0.78 we can derive a diel profile for $J_{C_{10}H_{17}NO_4}$ (Fig. S9). The maximum photolysis frequency is $\sim 2.2 \times 10^{-4}$ s^{-1} (at 10 UTC), which translates to a lifetime of 75 minutes. The average lifetime (over the entire diel profile) is 3.2 h and thus comparable to the deposition lifetimes of organic nitrates from BVOC.[9,14] In Fig. S9 we also display the atmospheric photolysis frequency using our actinic flux measurements but using the Wang *et al.*[31] cross sections (without extrapolation to longer wavelengths) and their quantum yield (0.071). The maximum photolysis frequency thus obtained is 2.8×10^{-5} s^{-1} which is very similar to their reported value ($3.0 \pm 1.5 \times 10^{-5}$ s^{-1}) obtained using the TUV model for a solar zenith angle of 28.14° (12:00 solar time, 1 August at 33.7° Latitude north (Atlanta, overhead O_3 column 300 Dobson units and albedo 0.1). The factor 7.8 larger value obtained in this work is thus clearly related to the larger quantum yield (0.78 from this work and 0.071 by Wang *et al.*[31]).

3.5. Photolysis of $C_{10}H_{16}N_2O_6$

A simpler analysis was performed for the di-nitrate ($C_{10}H_{16}N_2O_6$), whose temporal evolution under irradiation is shown in Fig. 8. Similar to the analysis above, in the presence of cyclohexane, we assume that the loss of $C_{10}H_{16}N_2O_6$ occurs only by photolysis and chamber outflow and is described by:

$$[C_{10}H_{16}N_2O_6]_t = [C_{10}H_{16}N_2O_6]_0 \times \exp - (J_{C_{10}H_{16}N_2O_6} + k_{exch})\, t \quad (6)$$

For $C_{10}H_{16}N_2O_6$, the fit to the data according to eqn (6) results in a loss constant in the presence of cyclohexane of 3.22×10^{-4} s^{-1}. Using the chamber exchange constant ($k_{exch} = 2.00 \times 10^{-4}$ s^{-1}) we derive $J_{C_{10}H_{16}N_2O_6} = (1.22 \pm 0.06) \times 10^{-4}$ s^{-1}. This value is lower than that obtained for the mono-nitrate $C_{10}H_{17}NO_4$ ($J_{C_{10}H_{17}NO_4} = (1.69 \pm 0.06) \times 10^{-4}$ s^{-1}), indicating a slower photochemical loss (photolysis lifetime = 2.3 h) of the di-nitrate at the wavelengths emitted by our LEDs (λ = 355–400 nm). However, in the absence of an absorption spectrum for $C_{10}H_{16}N_2O_6$, the available data do not allow a more detailed quantitative interpretation of this difference and we can only conclude that, like $C_{10}H_{17}NO_4$, the lifetime of $C_{10}H_{16}N_2O_6$ is strongly influenced by its photolysis.

3.6. Other LIM-ONO$_2$

Fig. S10 shows a time series of 13 LIM-ONO$_2$ species and NO_2. During the irradiation period (yellow shaded area) in the

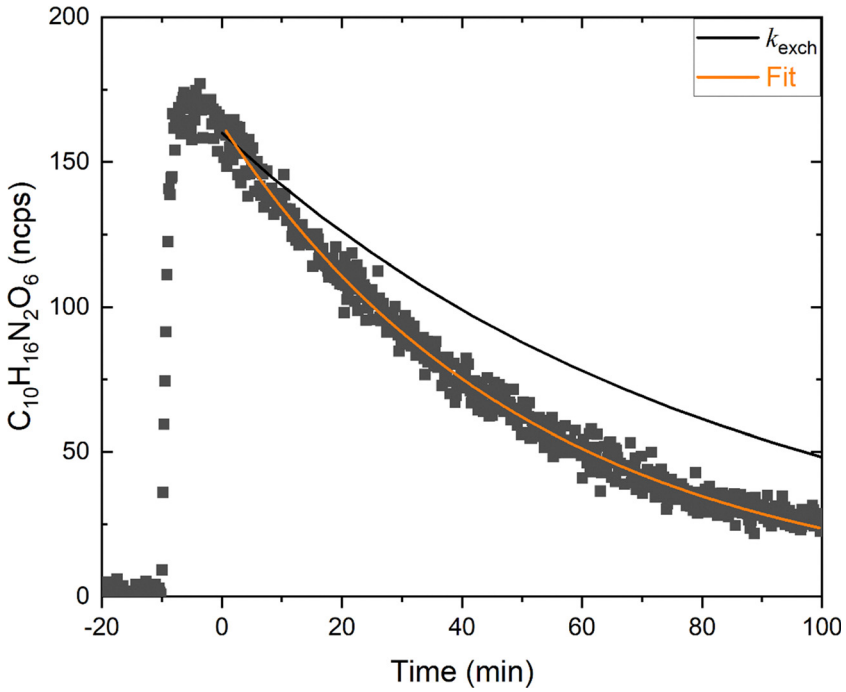

Fig. 8 Time-dependent signal of $C_{10}H_{16}N_2O_6$ during a photolysis experiment with cyclohexane as OH scavenger. The LEDs were switched on at Time = 0 min. The black line is calculated from the exchange rate constant k_{exch}. The orange line shows the first-order exponential fit to the data during photolysis with the decay constant given by 3.22×10^{-4} s^{-1}.

presence of cyclohexane, we observe that the mixing ratios of the LIM-ONO_2 species with the strongest HR-ToF-ICIMS signal ($C_{10}H_{17}NO_4$) decrease, as does that of the di-nitrate $C_{10}H_{16}N_2O_6$, both of which are treated in detail above. In contrast to the photolytic loss of $C_{10}H_{17}NO_4$ and $C_{10}H_{16}N_2O_6$, the mixing ratios of several shorter-chain nitrates (C2-9) increase during illumination as do those of some C10 nitrates (*i.e.* $C_{10}H_{13}NO_5$, $C_{10}H_{15}NO_5$, $C_{10}H_{17}NO_6$). The formation of shorter-chain nitrates appears to be consistent with the observations of Takeuchi *et al.*[53] who reported their production during photolysis of organic nitrates formed from α-pinene and β-pinene oxidation by the OH and NO_3 radicals. The formation of shorter chain nitrates could be understood if dissociative absorption leads not only to O–NO_2 bond fission but also to fission of a C(O)–C bond or if secondary reactions of the alkoxy radical formed in the primary photolysis step undergo further reactions that result in C–C bond fission. The increase in the signals of several C10-nitrates (notably $C_{10}H_{15}NO_5$, $C_{10}H_{15}NO_6$ and $C_{10}H_{15}NO_7$) can be explained by reactions of an initially formed alkoxy radical with O_2 to form a peroxy radical that can reform a nitrate *via* reaction with NO. Indeed, the main product of $C_{10}H_{17}NO_4$ photolysis observed by Wang *et al.*[31] was $C_{10}H_{17}NO_5$. Which was attributed to formation of the $C_{10}H_{17}O_2$ alkoxy radical and its decomposition and reaction with O_2 in the presence of NO. The photolytic formation of C10-nitrates is potentially also explained if the RO_2 + RO_2 reactions that produce the nitrated products described above also form peroxides (C10 "dimers") of the form ROOR (C20), which can dissociate by O–O bond fission. These ROOR have very low volatility and are likely to stick to the walls of the chamber or form particles rather than reside in the gas-phase. Previous studies have observed the formation of *e.g.* C20 dimers from the reaction of limonene with NO_3 radicals, primarily as highly oxygenated organic molecules in both the gas and particle phases.[23,24] The fact that we did not observe particles does not rule out the presence of very small particles formed by coagulation of ROOR type molecules and not detected by the CPC. ROOR dimers cannot be reliably identified with our HR-ToF-ICIMS due to the limited mass calibration range and the low sensitivity to C20 compounds. However, their low volatility means they would be collected efficiently in the cold-trap and re-injected into the SCHARK chamber. ROOR formed from NO_3 + limonene are likely reservoirs of C10 nitrates in our experiments, and their photolysis (either in the gas-phase or adsorbed on the chamber walls) is a potential explanation for some of the observed formation of C10 nitrates under irradiation in the SCHARK chamber.

4. Conclusions

In this study, we investigated the formation, isolation and photolysis of limonene-derived organic nitrates under controlled chamber conditions. Multifunctional organic nitrates formed from the reaction of limonene with NO_3 were successfully trapped at −30 °C, without co-condensation of limonene, allowing their re-injection into the chamber for photochemical investigation. By comparing the total multifunctional alkyl nitrates (in pptv) measured by the TD-CRDS with the summed HR-ToF-ICIMS signals (in ncps) of the individual organic

nitrates and assuming equal sensitivity of the HR-ToF-ICIMS to all detected LIM-ONO_2, we estimated the HR-ToF-ICIMS sensitivity as 21 ncps $pptv^{-1}$.

Our experimental approach further enabled the determination of in-chamber (λ = 355–400 nm) photolysis frequencies of $(1.69 \pm 0.06) \times 10^{-4}$ s^{-1} and $(1.22 \pm 0.06) \times 10^{-4}$ s^{-1} for $C_{10}H_{17}NO_4$ and $C_{10}H_{16}N_2O_6$, respectively. Photolysis of the re-injected limonene-derived organic nitrates led to the formation of shorter-chain nitrates (and an increase in NO_2). Using a chemical actinometer (Cl_2), with a photolysis frequency of $(1.99 \pm 0.007) \times 10^{-3}$ s^{-1} under our irradiation conditions we derived $J_{C_{10}H_{17}NO_4}/J_{Cl_2}$ = 0.085. From this ratio and assuming a quantum yield of unity, we derive a wavelength-averaged absorption cross section of 6.72×10^{-21} cm^2 $molecule^{-1}$ for $C_{10}H_{17}NO_4$ which agrees to within 25% with the cross section extrapolated from the solution-phase spectrum reported by Wang *et al.*[31] Alternatively, using different extrapolations of the Wang *et al.* cross-sections, we could estimate the quantum yield to be between 0.3 and 0.8. Our results demonstrate that $C_{10}H_{17}NO_4$ and $C_{10}H_{16}N_2O_6$ are photolabile limonene-derived nitrates that undergo photochemical loss at near-UV wavelengths. The measured photolysis lifetimes of 1.6 h and 2.3 h for $C_{10}H_{17}NO_4$ and $C_{10}H_{16}N_2O_6$, respectively, under chamber conditions indicates much faster degradation than previously reported for $C_{10}H_{17}NO_4$.[31] For ambient conditions we derived an averaged diel photolysis frequency of $C_{10}H_{17}NO_4$ of 8.5×10^{-5} s^{-1} (corresponding to a photolysis lifetime of 3.2 h) which is comparable to other physical sinks (*e.g.* dry deposition).

Author contributions

Conceptualization: JNC. Data curation: LW, LM, EJ, JS. Formal analysis: LW. Funding acquisition: JL, UP, JNC. Methodology: LW, JNC. Project administration: JNC. Resources: FD, JW, UP, JNC, JL. Supervision: PD, JNC. Validation: JNC. Visualization: LW. Writing – original draft: LW. Writing – review & editing: LW, LM, PD, EJ, JS, JW, FD, UP, JL, JNC.

Conflicts of interest

There are no conflicts to declare.

Data availability

The data underlying the figures in this publication are available at the Max Planck repository (EDMOND) at https://doi.org/10.17617/3.NHP25R.

Supplementary information is available. See DOI: https://doi.org/10.1039/d6cp00964f.

Acknowledgements

LM was funded by the Deutsche Forschungsgemeinschaft (DFG, German Research Foundation) – TRR 301 "TPChange" (Project-ID 428312742). PD gratefully acknowledges funding from the Deutsche Forschungsgemeinschaft (project "MONOTONS", project number: 522970430). Open Access funding provided by the Max Planck Society.

References

1 J. Williams, *Environ. Chem.*, 2004, **1**, 125.
2 A. B. Guenther, X. Jiang, C. L. Heald, T. Sakulyanontvittaya, T. Duhl, L. K. Emmons and X. Wang, *Geosci. Model Dev.*, 2012, **5**, 1471.
3 N. L. Ng, S. S. Brown, A. T. Archibald, E. Atlas, R. C. Cohen, J. N. Crowley, D. A. Day, N. M. Donahue, J. L. Fry, H. Fuchs, R. J. Griffin, M. I. Guzman, H. Herrmann, A. Hodzic, Y. Iinuma, J. L. Jimenez, A. Kiendler-Scharr, B. H. Lee, D. J. Luecken, J. Mao, R. McLaren, A. Mutzel, H. D. Osthoff, B. Ouyang, B. Picquet-Varrault, U. Platt, H. O. T. Pye, Y. Rudich, R. H. Schwantes, M. Shiraiwa, J. Stutz, J. A. Thornton, A. Tilgner, B. J. Williams and R. A. Zaveri, *Atmos. Chem. Phys.*, 2017, **17**, 2103.
4 D. Mogensen, R. Gierens, J. N. Crowley, P. Keronen, S. Smolander, A. Sogachev, A. C. Nölscher, L. Zhou, M. Kulmala, M. J. Tang, J. Williams and M. Boy, *Atmos. Chem. Phys.*, 2015, **15**, 3909.
5 J. M. Liebmann, G. Schuster, J. B. Schuladen, N. Sobanski, J. Lelieveld and J. N. Crowley, *Atmos. Meas. Tech.*, 2017, **10**, 1241.
6 R. P. Wayne, I. Barnes, P. Biggs, J. P. Burrows, C. E. Canosa-Mas, J. Hjorth, G. Le Bras, G. K. Moortgat, D. Perner, G. Poulet, G. Restelli and H. Sidebottom, *Atmos. Environ., Part A*, 1991, **25A**, 1.
7 P. O. Wennberg, K. H. Bates, J. D. Crounse, L. G. Dodson, R. C. McVay, L. A. Mertens, T. B. Nguyen, E. Praske, R. H. Schwantes, M. D. Smarte, J. M. St Clair, A. P. Teng, X. Zhang and J. H. Seinfeld, *Chem. Rev.*, 2018, **118**, 3337.
8 J. M. Roberts, *Atmos. Environ., Part A*, 1990, **24**, 243.
9 S. T. Andersen, R. Sander, P. Dewald, L. Wüst, T. Seubert, G. N. T. E. Türk, J. Schuladen, M. R. McGillen, C. Xue, A. Mellouki, A. Kukui, V. Michoud, M. Cirtog, M. Cazaunau, A. Bauville, H. Bouzidi, P. Formenti, C. Denjean, J. C. Etienne, O. Garrouste, C. Cantrell, J. Lelieveld and J. N. Crowley, *Atmos. Chem. Phys.*, 2025, **25**, 5893.
10 A. Zare, P. S. Romer, T. Nguyen, F. N. Keutsch, K. Skog and R. C. Cohen, *Atmos. Chem. Phys.*, 2018, **18**, 15419.
11 E. C. Browne, K. E. Min, P. J. Wooldridge, E. Apel, D. R. Blake, W. H. Brune, C. A. Cantrell, M. J. Cubison, G. S. Diskin, J. L. Jimenez, A. J. Weinheimer, P. O. Wennberg, A. Wisthaler and R. C. Cohen, *Atmos. Chem. Phys.*, 2013, **13**, 4543.
12 J. A. Fisher, D. J. Jacob, K. R. Travis, P. S. Kim, E. A. Marais, C. Chan Miller, K. Yu, L. Zhu, R. M. Yantosca, M. P. Sulprizio, J. Mao, P. O. Wennberg, J. D. Crounse, A. P. Teng, T. B. Nguyen, J. M. Clair, R. C. Cohen, P. Romer, B. A. Nault, P. J. Wooldridge, J. L. Jimenez, P. Campuzano-Jost, D. A. Day, W. Hu, P. B. Shepson, F. Xiong, D. R. Blake, A. H. Goldstein, P. K. Misztal, T. F. Hanisco, G. M. Wolfe, T. B. Ryerson, A. Wisthaler and T. Mikoviny, *Atmos. Chem. Phys.*, 2016, **16**, 5969.

13 J. Liebmann, E. Karu, N. Sobanski, J. Schuladen, M. Ehn, S. Schallhart, L. Quéléver, H. Hellen, H. Hakola, T. Hoffmann, J. Williams, H. Fischer, J. Lelieveld and J. N. Crowley, *Atmos. Chem. Phys.*, 2018, 3799.
14 J. Liebmann, N. Sobanski, J. Schuladen, E. Karu, H. Hellén, H. Hakola, Q. Zha, M. Ehn, M. Riva, L. Heikkinen, J. Williams, H. Fischer, J. Lelieveld and J. N. Crowley, *Atmos. Chem. Phys.*, 2019, **19**, 10391.
15 P. Dewald, T. Seubert, S. T. Andersen, G. N. T. E. Türk, J. Schuladen, M. R. McGillen, C. Denjean, J. C. Etienne, O. Garrouste, M. Jamar, S. Harb, M. Cirtog, V. Michoud, M. Cazaunau, A. Bergé, C. Cantrell, S. Dusanter, B. Picquet-Varrault, A. Kukui, C. Xue, A. Mellouki, J. Lelieveld and J. N. Crowley, *Atmos. Chem. Phys.*, 2024, **24**, 8983.
16 H. Hellén, A. P. Praplan, T. Tykkä, I. Ylivinkka, V. Vakkari, J. Bäck, T. Petäjä, M. Kulmala and H. Hakola, *Atmos. Chem. Phys.*, 2018, **18**, 13839.
17 D. F. McGlynn, L. E. R. Barry, M. T. Lerdau, S. E. Pusede and G. Isaacman-VanWertz, *Atmos. Chem. Phys.*, 2021, **21**, 15755.
18 M. Ammann, R. A. Cox, J. N. Crowley, H. Herrmann, M. E. Jenkin, V. F. McNeill, A. Mellouki, M. J. Rossi, J. Troe and T. J. Wallington, IUPAC, IUPAC Task Group on Atmospheric Chemical Kinetic Data Evaluation, Last access March 2026, https://iupac.aeris-data.fr/.
19 J. L. Fry, A. Kiendler-Scharr, A. W. Rollins, T. Brauers, S. S. Brown, H. P. Dorn, W. P. Dube, H. Fuchs, A. Mensah, F. Rohrer, R. Tillmann, A. Wahner, P. J. Wooldridge and R. C. Cohen, *Atmos. Chem. Phys.*, 2011, **11**, 3879.
20 M. Hallquist, I. Wangberg, E. Ljungstrom, I. Barnes and K. H. Becker, *Environ. Sci. Technol.*, 1999, **33**, 553.
21 A. Mutzel, Y. Zhang, O. Böge, M. Rodigast, A. Kolodziejczyk, X. Wang and H. Herrmann, *Atmos. Chem. Phys.*, 2021, **21**, 8479.
22 M. P. DeVault, A. C. Ziola and P. J. Ziemann, *ACS Earth Space Chem.*, 2022, **6**, 2076.
23 Y. Guo, H. Shen, I. Pullinen, H. Luo, S. Kang, L. Vereecken, H. Fuchs, M. Hallquist, I. H. Acir, R. Tillmann, F. Rohrer, J. Wildt, A. Kiendler-Scharr, A. Wahner, D. Zhao and T. F. Mentel, *Atmos. Chem. Phys.*, 2022, **22**, 11323.
24 C. Faxon, J. Hammes, M. Le Breton, R. K. Pathak and M. Hallquist, *Atmos. Chem. Phys.*, 2018, **18**, 5467.
25 R. Mayorga, Y. Xia, Z. Zhao, B. Long and H. Zhang, *Environ. Sci. Technol.*, 2022, **56**, 15337.
26 F. L. Z. Xiong, C. H. Borca, L. V. Slipchenko and P. B. Shepson, *Atmos. Chem. Phys.*, 2016, **16**, 5595.
27 J. F. Muller, J. Peeters and T. Stavrakou, *Atmos. Chem. Phys.*, 2014, **14**, 2497.
28 K. C. Clemitshaw, J. Williams, O. V. Rattigan, D. E. Shallcross, K. S. Law and R. Anthony Cox, *J. Photochem. Photobiol., A*, 1997, **102**, 117.
29 J. M. Roberts and R. W. Fajer, *Environ. Sci. Technol.*, 1989, **23**, 945.
30 I. Barnes, K. H. Becker and T. Zhu, *J. Atmos. Chem.*, 1993, **17**, 353.
31 Y. Wang, M. Takeuchi, S. Wang, S. A. Nizkorodov, S. France, G. Eris and N. L. Ng, *J. Phys. Chem. A*, 2023, **127**, 987.
32 Y. Wang, I. R. Piletic, M. Takeuchi, T. Xu, S. France and N. L. Ng, *Environ. Sci. Technol.*, 2021, **55**, 14595.
33 R. Suarez-Bertoa, B. Picquet-Varrault, W. Tamas, E. Pangui and J. F. Doussin, *Environ. Sci. Technol.*, 2012, **46**, 12502.
34 B. Picquet-Varrault, R. Suarez-Bertoa, M. Duncianu, M. Cazaunau, E. Pangui, M. David and J. F. Doussin, *Atmos. Chem. Phys.*, 2020, **20**, 487.
35 L. Wüst, P. Dewald, G. N. T. E. Türk, J. Lelieveld and J. N. Crowley, *Atmos. Meas. Tech.*, 2025, **18**, 1943.
36 P. Dewald, R. Dörich, J. Schuladen, J. Lelieveld and J. N. Crowley, *Atmos. Meas. Tech.*, 2021, **14**, 5501.
37 B. H. Lee, F. D. Lopez-Hilfiker, C. Mohr, T. Kurten, D. R. Worsnop and J. A. Thornton, *Environ. Sci. Technol.*, 2014, **48**, 6309.
38 Y. Ji, L. G. Huey, D. J. Tanner, Y. R. Lee, P. R. Veres, J. A. Neuman, Y. Wang and X. Wang, *Atmos. Meas. Tech.*, 2020, **13**, 3683.
39 L. Moorman, J. N. Crowley, F. Fachinger and F. Drewnick, *Environ. Sci.: Atmos.*, 2026, **6**, 579.
40 N. Sobanski, M. J. Tang, J. Thieser, G. Schuster, D. Pöhler, H. Fischer, W. Song, C. Sauvage, J. Williams, J. Fachinger, F. Berkes, P. Hoor, U. Platt, J. Lelieveld and J. N. Crowley, *Atmos. Chem. Phys.*, 2016, **16**, 4867.
41 A. C. Vandaele, C. Hermans, P. C. Simon, M. Carleer, R. Colin, S. Fally, M. F. Merienne, A. Jenouvrier and B. Coquart, *J. Quant. Spectrosc. Radiat. Transfer*, 1998, **59**, 171.
42 N. Sobanski, J. Schuladen, G. Schuster, J. Lelieveld and J. N. Crowley, *Atmos. Meas. Tech.*, 2016, **9**, 5103.
43 J. A. Davidson, A. A. Viggiano, C. J. Howard, I. Dotan, F. C. Fehsenfeld, D. L. Albritton and E. E. Ferguson, *J. Chem. Phys.*, 1978, **68**, 2085.
44 N. M. Donahue, S. A. Epstein, S. N. Pandis and A. L. Robinson, *Atmos. Chem. Phys.*, 2011, **11**, 3303.
45 Y. Li, U. Pöschl and M. Shiraiwa, *Atmos. Chem. Phys.*, 2016, **16**, 3327.
46 B. R. Ayres, H. M. Allen, D. C. Draper, S. S. Brown, R. J. Wild, J. L. Jimenez, D. A. Day, P. Campuzano-Jost, W. Hu, J. de Gouw, A. Koss, R. C. Cohen, K. C. Duffey, P. Romer, K. Baumann, E. Edgerton, S. Takahama, J. A. Thornton, B. H. Lee, F. D. Lopez-Hilfiker, C. Mohr, P. O. Wennberg, T. B. Nguyen, A. Teng, A. H. Goldstein, K. Olson and J. L. Fry, *Atmos. Chem. Phys.*, 2015, **15**, 13377.
47 M. Takeuchi, T. Berkemeier, G. Eris and N. L. Ng, *Nat. Commun.*, 2022, **13**, 7883.
48 S. Aggarwal, P. Bansal, Y. Wang, S. Jorga, G. Macgregor, U. Rohner, T. Bannan, M. Salter, P. Zieger, C. Mohr and F. Lopez-Hilfiker, *Atmos. Meas. Tech.*, 2025, **18**, 4227.
49 F. D. Lopez-Hilfiker, S. Iyer, C. Mohr, B. H. Lee, E. L. D'Ambro, T. Kurtén and J. A. Thornton, *Atmos. Meas. Tech.*, 2016, **9**, 1505.
50 E. Bourtsoukidis, F. Helleis, L. Tomsche, H. Fischer, R. Hofmann, J. Lelieveld and J. Williams, *Atmos. Meas. Tech.*, 2017, **10**, 5089.
51 F. Rohrer, B. Bohn, D. Brüning, F.-J. Johnen, A. Wahner and J. Kleffmann, *ACP*, 2005, **5**, 2189.
52 D. Maric, J. P. Burrows, R. Meller and G. K. Moortgat, *J. Photochem. Photobiol., A*, 1993, **70**, 205.
53 M. Takeuchi, Y. Wang and N. L. Ng, *ACS EST Air*, 2025, **2**, 2445.